A locking-free stabilized kinematic EFG model for plane strain limit analysis

Canh V. Le [a], H. Askes [b] and M. Gilbert [b,*]

[a] *Department of Civil Engineering, International University, VNU HCMC, Vietnam.*

[b] *Department of Civil and Structural Engineering, The University of Sheffield, United Kingdom.*

Abstract

An Element Free Galerkin (EFG) based formulation for limit analysis of rigid-perfectly plastic plane strain problems is presented. In the paper it is demonstrated that volumetric locking and instability problems can be avoided by using a stabilized conforming nodal integration scheme. Furthermore, the stabilized EFG method described allows stable and accurate solutions to be obtained with minimal computational effort. The discrete kinematic formulation is cast in the form of a second-order cone problem, allowing efficient interior-point solvers to be used to obtain solutions. Finally, the performance of the stabilized EFG method is illustrated by considering several numerical examples.

Key words: Limit analysis; meshless methods; volumetric locking; strain smoothing; nodal integration; second order cone programming.

1 INTRODUCTION

The load required to cause collapse of a body or structure can be directly estimated using limit analysis. Considering an upper-bound kinematic limit analysis approach, the flow rule is required to be satisfied everywhere in the problem domain. This requirement can easily be met using constant strain

* Corresponding author
Email addresses: lvcanh@hcmiu.edu.vn (Canh V. Le), h.askes@sheffield.ac.uk (H. Askes), m.gilbert@sheffield.ac.uk (M. Gilbert).

finite elements. However, it is well-known that such elements exhibit volumetric locking phenomena when used in conjunction with von Mises or Tresca yield criteria, due to the large number of incompressibility constraints imposed on the nodal velocities [1–3]. Various solutions have been proposed in the literature to overcome this problem. These include the use of higher-order displacement-based finite elements [3,4], mixed formulations [2,5–7] and kinematic formulations using discontinuous velocity fields [8–10]. Additionally a fully discontinuous formulation which involves identification of the critical layout of discontinuities at failure has been proposed [11].

Recently, Le et al. [12] proposed a numerical kinematic formulation using the cell-based smoothed finite element method (SFEM) and second-order cone programming (SOCP) to prevent the volumetric locking problem, and also to furnish good (approximate) upper-bound solutions for plane strain problems governed by the von Mises failure criterion. Alternately, meshfree methods can be used. The Element-Free Galerkin (EFG) method, one of the first meshfree approaches, has been applied successfully to a wide range of computational problems, proving popular due to its naturally conforming property (with no nodal connectivity required) and its rapid convergence characteristics [13]. The EFG method has also been applied successfully to limit analysis problems [14–16]. It has been shown that the EFG method is in general well suited for limit analysis problems, allowing accurate solutions to be obtained with relatively few degrees of freedom. Following this line of research, the main objective of this paper is to investigate the performance of a stabilized EFG method when applied to plane strain limit analysis problems, where volumetric locking can occur as a result of the use of an unbounded yield criterion.

Volumetric (or 'isochoric') locking is caused by the use of approximations which prevent certain velocity fields from being exactly described [17]. When low-order finite elements are used, the kinematic constraint (or 'divergence-free' or 'incompressibility' condition) leads to a reduction in the available number of degrees of freedom, and therefore the true velocity field cannot be exactly described. However, meshfree methods generally provide high-order shape functions [13,18], and therefore volumetric locking in elasto-plastic analysis problems can be suppressed by increasing the so-called dilation parameter [17,19,20], though not entirely removed [21]. The locking problem can also be relieved by using direct nodal integration or collocation methods, but these methods often result in rank deficiency and thus can produce spurious singular modes [22,23]. In order to eliminate the spatial instabilities associated with nodal integration, a stabilized conforming nodal integration (SCNI) has been proposed in [24], which has then been applied successfully to various problems [16,23,25,26]; see also [27] for a description of how kinematic and equilibrium approaches can be used in combination to closely bracket the exact solution for plate problems. In the present paper, which focuses on plane strain problems, it will be shown that when the SCNI scheme is employed

in the EFG-based kinematic formulation, the solutions obtained are accurate and stable, and volumetric locking can also be prevented.

This paper is organized as follows: In the next section, the kinematic limit analysis formulation is briefly reviewed. The approximation used to describe the displacement field and the SCNI smoothing technique are then presented, and the discrete formulation is also given. In Section 4, the underlying optimization problem is cast in the form of a second-order cone problem, allowing efficient interior-point solvers to be used to obtain solutions. Numerical examples are provided in Section 5 to illustrate the ability of the proposed method to prevent volumetric locking, and approximated upper bound solutions are then compared with those in the literature.

2 KINEMATIC LIMIT ANALYSIS

Consider a rigid-perfectly plastic body of area $\Omega \in \mathbb{R}^2$ with boundary Γ, which is subjected to body forces f and to surface tractions g on the free portion Γ_t of Γ. The constrained boundary Γ_u is fixed and $\Gamma_u \cup \Gamma_t = \Gamma$, $\Gamma_u \cap \Gamma_t = \oslash$. Let $\dot{\mathbf{u}} = \begin{bmatrix} \dot{u} & \dot{v} \end{bmatrix}^T$ be the velocity or flow fields that belong to a space Y of kinematically admissible velocity fields, where $\dot{u}$ and $\dot{v}$ are the velocity components in the x- and y-directions respectively.

The external work rate associated with a virtual plastic flow $\dot{\mathbf{u}}$ is expressed in linear form as

$$F(\dot{\mathbf{u}}) = \int_{\Omega} \mathbf{f}^T \dot{\mathbf{u}} \, \mathrm{d}\Omega + \int_{\Gamma_t} \mathbf{g}^T \dot{\mathbf{u}} \, \mathrm{d}\Gamma \tag{1}$$

If $C = \{\dot{\mathbf{u}} \in Y \mid F(\dot{\mathbf{u}}) = 1\}$, then the collapse load multiplier λ can be determined by solving the following mathematical programming problem

$$\lambda^+ = \min_{\dot{\mathbf{u}} \in C} \int_{\Omega} D(\dot{\boldsymbol{\epsilon}}) \, \mathrm{d}\Omega \tag{2}$$

where strain rates $\dot{\boldsymbol{\epsilon}}$ are given by

$$\dot{\boldsymbol{\epsilon}} = \begin{bmatrix} \dot{\epsilon}_{xx} \\ \dot{\epsilon}_{yy} \\ \dot{\gamma}_{xy} \end{bmatrix} = \nabla \dot{\mathbf{u}} \tag{3}$$

and where the differential operator ∇ is given by

$$\nabla = \begin{bmatrix} \dfrac{\partial}{\partial x} & 0 \\ 0 & \dfrac{\partial}{\partial y} \\ \dfrac{\partial}{\partial y} & \dfrac{\partial}{\partial x} \end{bmatrix} \tag{4}$$

The plastic dissipation $D(\dot{\boldsymbol{\epsilon}})$ is defined by

$$D(\dot{\boldsymbol{\epsilon}}) = \max_{\psi(\boldsymbol{\sigma})\leq 0} \boldsymbol{\sigma} : \dot{\boldsymbol{\epsilon}} \equiv \boldsymbol{\sigma}_{\epsilon} : \dot{\boldsymbol{\epsilon}} \tag{5}$$

in which $\boldsymbol{\sigma}$ represents the admissible stresses contained within the convex yield surface and $\boldsymbol{\sigma}_{\epsilon}$ represents the stresses on the yield surface associated with any strain rates $\dot{\boldsymbol{\epsilon}}$ through the plasticity condition.

In the framework of a limit analysis problem, only plastic strains are considered and are assumed to obey the normality rule

$$\dot{\boldsymbol{\epsilon}} = \dot{\mu}\frac{\partial \psi}{\partial \boldsymbol{\sigma}} \tag{6}$$

where the plastic multiplier $\dot{\mu}$ is non-negative and the yield function $\psi(\boldsymbol{\sigma})$ is convex. In this study the von Mises failure criterion is used (which is equivalent to the Tresca criterion in plane strain [5]). Thus

$$\psi(\boldsymbol{\sigma}) = \sqrt{\frac{1}{4}(\sigma_{xx} - \sigma_{yy})^2 + \sigma_{xy}^2} - \sigma_0 \tag{7}$$

where σ_0 is the yield stress.

Then the power of dissipation can be formulated as a function of strain rates as [5]

$$D(\dot{\boldsymbol{\epsilon}}) = \sigma_0\sqrt{\dot{\boldsymbol{\epsilon}}^T \boldsymbol{\Theta}\, \dot{\boldsymbol{\epsilon}}} \tag{8}$$

where

$$\boldsymbol{\Theta} = \begin{bmatrix} 1 & -1 & 0 \\ -1 & 1 & 0 \\ 0 & 0 & 1 \end{bmatrix} \tag{9}$$

Note that condition (6) acts as a kinematic constraint which confines admissible strain rate vectors. Since the yield surface $\psi(\boldsymbol{\sigma})$ is unbounded, the incompressibility condition $\boldsymbol{\chi}^T\dot{\boldsymbol{\epsilon}} = 0$, where $\boldsymbol{\chi} = \begin{bmatrix} 1 & 1 & 0 \end{bmatrix}^T$, must be introduced to ensure that the plastic dissipation $D(\dot{\boldsymbol{\epsilon}})$ is finite [2,6,28,29].

3 EFG DISCRETIZATION OF KINEMATIC FORMULATION

3.1 Moving least squares approximation

By using the moving least squares technique [13,30], which is one of the most frequently used approximations in meshless methods, approximations of the displacement (or displacement rate) fields can be expressed as

$$\mathbf{u}^h(\mathbf{x}) = \begin{bmatrix} u^h \\ v^h \end{bmatrix} = \sum_{I=1}^{n} \Phi_I(\mathbf{x}) \begin{bmatrix} u_I \\ v_I \end{bmatrix} \tag{10}$$

in which

$$\Phi_I(\mathbf{x}) = \mathbf{p}^T(\mathbf{x})\mathbf{A}^{-1}(\mathbf{x})\mathbf{B}_I(\mathbf{x}) \tag{11}$$

$$\mathbf{A}(\mathbf{x}) = \sum_{I=1}^{n} w_I(\mathbf{x})\mathbf{p}(\mathbf{x}_I)\mathbf{p}^T(\mathbf{x}_I) \tag{12}$$

$$\mathbf{B}_I(\mathbf{x}) = w_I(\mathbf{x})\mathbf{p}(\mathbf{x}_I) \tag{13}$$

where n is the number of nodes; $\mathbf{p}(\mathbf{x})$ is a set of basis functions and $w_I(\mathbf{x})$ is a weight function associated with node I. In this work, an isotropic quartic spline function is used, which is given by

$$w_I(\mathbf{x}) = \begin{cases} 1 - 6s_I^2 + 8s_I^3 - 3s_I^4 \text{ if } s_I \leq 1 \\ 0 \qquad\qquad\qquad\qquad\quad \text{if } s_I > 1 \end{cases} \tag{14}$$

with $s_I = \frac{\|\mathbf{x}-\mathbf{x}_I\|}{R_I}$, where R_I is the support radius of node I and determined by

$$R_I = \beta \cdot h_I \tag{15}$$

where β is the dimensionless size of influence domain and h_I is the nodal spacing when nodes are distributed regularly, or the maximum distance to neighbouring nodes when nodes are distributed irregularly; further details can be found in [15]. In the next section, a technique will be presented that allows the required order of differentiation to be reduced by one, with the consequence that there is no need to calculate shape function derivatives for the stabilized EFG formulation.

3.2 Strain smoothing stabilization

A strain smoothing method was firstly presented in [31] for regularization of material instabilities. The strain smoothing method was then modified for

stabilization of nodal integration by [24]

$$\tilde{\epsilon}_{ij}^{h}(\mathbf{x}_J) = \int_{\Omega_J} \epsilon_{ij}^{h}(\mathbf{x})\varphi(\mathbf{x}, \mathbf{x} - \mathbf{x}_J)\, \mathrm{d}\Omega \tag{16}$$

where $\tilde{\epsilon}_{ij}^{h}$ is the smoothed value of strains ϵ_{ij}^{h} at node J, and φ is a distribution (or smoothing) function that has to satisfy the following properties [31,32]

$$\varphi \geq 0 \quad \text{and} \quad \int_{\Omega_J} \varphi \, \mathrm{d}\Omega = 1 \tag{17}$$

For simplicity, the smoothing function φ is assumed to be a piecewise constant function and is given by

$$\varphi(\mathbf{x}, \mathbf{x} - \mathbf{x}_J) = \begin{cases} 1/A_J, & \mathbf{x} \in \Omega_J \\ 0, & \mathbf{x} \notin \Omega_J \end{cases} \tag{18}$$

where A_J is the area of the representative domain of node J.

Substituting equation (18) into the equation (16), and applying the divergence theorem furnishes

$$\begin{aligned} \tilde{\epsilon}_{ij}^{h}(\mathbf{x}_J) &= \frac{1}{A_J} \int_{\Omega_J} \frac{1}{2}(u_{i,j}^{h} + u_{j,i}^{h})\, \mathrm{d}\Omega \\ &= \frac{1}{2A_J} \oint_{\Gamma_J} \left(u_i^h n_j + u_j^h n_i \right) \mathrm{d}\Omega \end{aligned} \tag{19}$$

where Γ_J is the boundary of the representative domain Ω_J.

Now introducing a moving least squares approximation of the displacement fields, the smooth version of the strains can be expressed as

$$\tilde{\boldsymbol{\epsilon}}^{h}(\mathbf{x}_J) = \begin{bmatrix} \tilde{\epsilon}_{xx}^{h}(\mathbf{x}_J) \\ \tilde{\epsilon}_{yy}^{h}(\mathbf{x}_J) \\ \tilde{\gamma}_{xy}^{h}(\mathbf{x}_J) \end{bmatrix} = \tilde{\mathbf{B}}\mathbf{d} \tag{20}$$

where

$$\mathbf{d}^T = [u_1, u_2, \ldots, u_n, v_1, v_2, \ldots, v_n] \tag{21}$$

$$\tilde{\mathbf{B}} = \begin{bmatrix} \tilde{\Phi}_{1,x} & \tilde{\Phi}_{2,x} & \ldots & \tilde{\Phi}_{n,x} & 0 & 0 & \ldots & 0 \\ 0 & 0 & \ldots & 0 & \tilde{\Phi}_{1,y} & \tilde{\Phi}_{2,y} & \ldots & \tilde{\Phi}_{n,y} \\ \tilde{\Phi}_{1,y} & \tilde{\Phi}_{2,y} & \ldots & \tilde{\Phi}_{n,y} & \tilde{\Phi}_{1,x} & \tilde{\Phi}_{2,x} & \ldots & \tilde{\Phi}_{n,x} \end{bmatrix} \tag{22}$$

with

$$\tilde{\Phi}_{I,\alpha}(\mathbf{x}_J) = \frac{1}{A_J} \oint_{\Gamma_J} \Phi_I(\mathbf{x}_J) n_\alpha(\mathbf{x}) \mathrm{d}\Gamma \tag{23}$$

The boundary integral on the RHS of Eq. (23) can be determined numerically using the technique presented in [24,33].

3.3 Kinematic limit analysis formulation

The internal dissipation power of the two-dimensional plane domain Ω can now be determined using a nodal integration scheme and moving least square approximation of the transverse displacement rates $\dot{\mathbf{u}}^h(\mathbf{x})$ as

$$D^{EFG} = \int_\Omega \sigma_0 \sqrt{\dot{\boldsymbol{\epsilon}}^{hT} \boldsymbol{\Theta}\, \dot{\boldsymbol{\epsilon}}^h}\, \mathrm{d}\Omega = \sum_{J=1}^{n} \sigma_0\, A_J \sqrt{\dot{\tilde{\boldsymbol{\epsilon}}}^{hT}(\mathbf{x}_J) \boldsymbol{\Theta}\, \dot{\tilde{\boldsymbol{\epsilon}}}^h(\mathbf{x}_J)} \tag{24}$$

The smoothed strain rates $\dot{\tilde{\boldsymbol{\epsilon}}}^h(\mathbf{x}_J)$ are also used to enforce the incompressibility condition, and hence the upper-bound limit analysis problem for plane strain problems can be formulated as

$$\begin{aligned} \lambda^+ = \min\ & \sum_{J=1}^{n} \sigma_0\, A_J \sqrt{\dot{\tilde{\boldsymbol{\epsilon}}}^{hT}(\mathbf{x}_J) \boldsymbol{\Theta}\, \dot{\tilde{\boldsymbol{\epsilon}}}^h(\mathbf{x}_J)} \\ \text{s.t} & \begin{cases} F(\dot{\mathbf{u}}^h) = 1 \\ \dot{\mathbf{u}}^h = \mathbf{0} \qquad\quad \text{on } \Gamma_u \\ \boldsymbol{\chi}^T \dot{\tilde{\boldsymbol{\epsilon}}}^h(\mathbf{x}_J) = 0 \;\; J = 1, 2, \ldots, n \end{cases} \end{aligned} \tag{25}$$

Note that the collocation method presented in [34] is used here to enforce essential boundary conditions. The nodal integration scheme is also used to determine the external energy $F(\dot{\mathbf{u}}^h)$. Furthermore, in order to obtain a strict upper bound solution, the incompressibility constraint in (25) is required to hold throughout the problem domain. In the present kinematic formulation, an isotropic quartic spline weight function is used in conjunction with a moving least-squares approximation, which results in a high-order of the approximated displacement field. This makes a proof of the strict bound status of the solutions difficult since the incompressibility condition can only be enforced at a finite number of points. Fortunately, when a stabilized conforming nodal integration is applied, the smoothed strain rates obtained are constant over a Voronoi cell. Therefore, the incompressibility constraint only needs to be enforced at any one point in each cell, and it is then guaranteed to be satisfied

everywhere in the problem domain. Although the strain rates obtained using the strain smoothing technique relax the compatibility constraints somewhat, affecting the strict boundedness of the solutions obtained, the collapse loads computed using the proposed method can under normal circumstances be expected to bound from above the corresponding exact values.

4 SOLUTION OF THE DISCRETE PROBLEM

The determinant of the matrix $\boldsymbol{\Theta}$ in Equation (9) is equal to zero and its Cholesky factor does not exist. Therefore, the technique used to formulate the dissipation function as a sum of norms, as presented in [15], cannot be applied here. However, it is still possible to transform (25) into a problem of minimizing a sum of norms, as follows.

First, the objective function in the above optimization problem is rewritten as

$$D^{EFG} = \sum_{J=1}^{n} \sigma_0 A_J \sqrt{\left(\dot{\tilde{\epsilon}}^h_{xx}(\mathbf{x}_J) - \dot{\tilde{\epsilon}}^h_{yy}(\mathbf{x}_J)\right)^2 + \left(\dot{\tilde{\gamma}}^h_{xy}(\mathbf{x}_J)\right)^2} \tag{26}$$

For convenience, a vector of additional variables $\boldsymbol{\rho}$ is introduced as

$$\boldsymbol{\rho} = \begin{bmatrix} \rho_1 \\ \\ \rho_2 \end{bmatrix} = \begin{bmatrix} \dot{\tilde{\epsilon}}^h_{xx}(\mathbf{x}_J) - \dot{\tilde{\epsilon}}^h_{yy}(\mathbf{x}_J) \\ \\ \dot{\tilde{\gamma}}^h_{xy}(\mathbf{x}_J) \end{bmatrix} \tag{27}$$

The plastic dissipation can then be expressed as

$$D^{EFG} = \sum_{J=1}^{n} \sigma_0 A_J \, ||\boldsymbol{\rho}|| \tag{28}$$

Now the optimization problem (25) becomes a problem of minimizing a sum of norms as

$$\begin{aligned} \lambda^+ = \min & \sum_{J=1}^{n} \sigma_0 \, A_J \, ||\boldsymbol{\rho}|| \\ \text{s.t} & \begin{cases} F(\dot{\mathbf{u}}^h) = 1 \\ \dot{\mathbf{u}}^h = \mathbf{0} \qquad\qquad \text{on } \Gamma_u \\ \boldsymbol{\chi}^T \dot{\tilde{\boldsymbol{\epsilon}}}^h(\mathbf{x}_J) = 0 \;\; J = 1, 2, \ldots, n \end{cases} \end{aligned} \tag{29}$$

In fact a problem of this sort can be cast as a second-order cone programming (SOCP) problem by introducing auxiliary variables $t_1,\ t_2,\ \ldots,\ t_n$

$$\lambda^+ = \min \sum_{j=1}^{n} \sigma_0 A_j t_j$$
$$\text{s.t} \begin{cases} F(\dot{\mathbf{u}}^h) = 1 \\ \dot{\mathbf{u}}^h = \mathbf{0} \qquad \text{on } \Gamma_u \\ \boldsymbol{\chi}^T \dot{\tilde{\boldsymbol{\epsilon}}}^h(\mathbf{x}_J) = 0 \;\; J = 1, 2, \ldots, n \\ ||\boldsymbol{\rho}||_i \leq t_i \qquad i = 1, 2, \ldots, n \end{cases} \tag{30}$$

where the fourth constraint in problem (30) represents quadratic cones, and $\boldsymbol{\rho}$ is defined by Equation (27). Note that the number of terms in the objective function is equal to the number of integration points. When Gauss integration is used, a large number of integration points would be needed in order to obtain accurate solutions. This results in an increased number of additional variables t_j and cones $\|\boldsymbol{\rho}\|_i \leq t_i$, and also in a large number of incompressibility constraints (the third constraint in Eq. 30), which may cause volumetric locking, as manifested in numerical results. In contrast, the SCNI scheme used here reduces the size of the resulting optimization problem, and locking problems can be avoided.

5 NUMERICAL EXAMPLES

The performance of the proposed solution procedure will be tested by examining a number of benchmark plane strain problems for which analytical or previous numerical solutions are available. Linear basis functions are used in the moving least squares approximation, and the parameter β in Equation (15) is set to be equal to 1.5 (note that whilst use of a higher value of β may sometimes lead to a better upper-bound solution, computational costs will increase with the size of the domain of influence).

5.1 Prandtl problem

The first example comprises the classical plane strain problem originally investigated by Prandtl [35], as shown in Figure 1. For a load of $2\tau_0$, the analytical collapse multiplier is $\lambda = 2 + \pi = 5.142$. The strong discontinuity at the edge of the indentor presents a severe challenge to many numerical analysis procedures.

Due to symmetry, only half the domain needs to be considered. A rectangular region of dimensions $B = 5$ and $H = 2$ was used and the indentor (or 'punch')

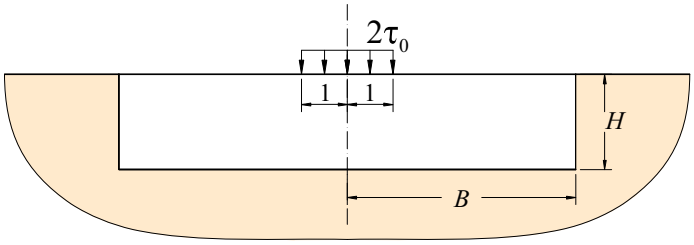

Fig. 1. Prandtl problem: geometry and loading

was represented by a uniform vertical load. Finally, appropriate boundary conditions were imposed, all as indicated in Figure 2.

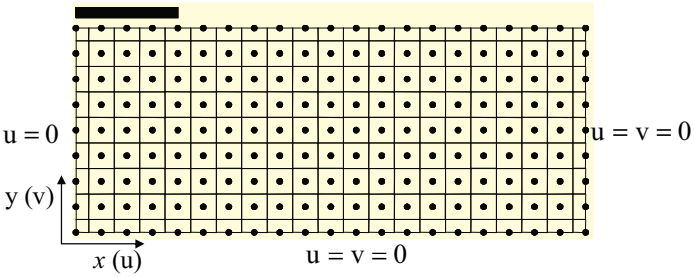

Fig. 2. Prandtl problem: nodal layout, Voronoi cells and displacement boundary conditions

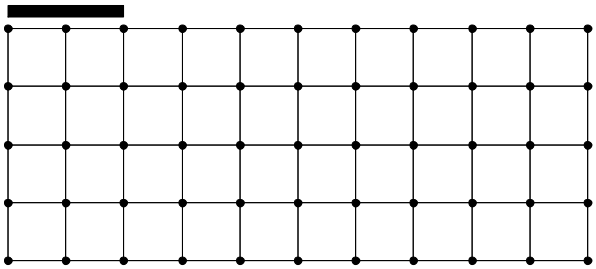

Fig. 3. Prandtl problem: background mesh for Gauss integration scheme

First, consider volumetric locking behavior. Three integration schemes were considered: (i) Gauss integration, (ii) direct nodal integration (DNI), and (iii) stabilized conforming nodal integration (SCNI). For the Gauss integration scheme, a background mesh is required, as shown on Figure 3. (Note that the EFG field nodes are independent of the background mesh). In order to measure volumetric locking a constraint ratio r will be defined as

$$r = \frac{n_{dof}}{n_{iCon}} \tag{31}$$

where n_{dof} is the total number of degrees of freedom and n_{iCon} is the number of incompressibility constraints imposed. Numerical results using various Gauss rules and different numbers of nodes are reported in Table 1.

Table 1
Prandtl problem: numerical results using Gauss integration

Gauss rule	N	2	4	6	8	10
	n_{dof}	55×2	189×2	403×2	697×2	1071×2
3×3	r	0.2730	0.9380	2.0000	under-integration	
	λ^+	inf	inf	5.2309	instability	
5×5	r	0.1027	0.3529	0.7526	1.3016	2.0000
	λ^+	inf	inf	inf	5.3060	5.1895
7×7	r	0.0534	0.1836	0.3915	0.6770	1.0403
	λ^+	inf	inf	inf	inf	5.2088

Key: N = number of divisions under the indentor
inf: no feasible solution satisfying all constraints; i.e. 'locking' occurred.

It can be observed from Table 1 that, when using Gauss integration, 'locking' problems occur when the constraint ratio r is smaller than 1. It is interesting to note that increasing the size of the domain of influence does not help in this case. However, it is evident that volumetric locking can be prevented if $r > 1$. (i.e. if the number of nodes is sufficiently large in comparison with the number of integration points.) Note that when $r = 2$ the number of nodes is equal to the number of integration points, resulting in direct nodal integration (DNI). Although DNI can prevent volumetric locking, spatial instabilities can occur. This problem becomes more serious if Gauss integration with $r > 2$ is used (i.e. under-integration). In contrast, in the SCNI scheme nodal values are determined by spatially averaging field values using the divergence theorem, and hence the spatial instability problem can be eliminated. Furthermore, when employing the same number of nodes it will be demonstrated that the collapse multiplier obtained using SCNI is generally much lower, and more accurate, than the solution obtained using DNI (e.g. 5.1595 compared with 5.2309 respectively when using 403×2 nodes - shown on Tables 2 and 1 respectively). In summary, there are two main advantages of using SCNI when treating plane strain limit analysis problems: (i) volumetric locking is prevented, and (ii) stable and accurate solutions can be obtained at little computational cost. Due to these advantages, the SCNI scheme will be employed for all problems considered hereafter.

Collapse multipliers and the corresponding errors for various nodal discretizations are given in Table 2. It can be observed that accurate solutions can be

obtained using the present method. In most cases the computed errors are smaller than 1%, and when only 189 nodes are used an extremely satisfactory solution can be obtained (0.69% error). Furthermore, it is evident that all solutions obtained are above the exact value for this problem. Although it has been pointed out that the procedure cannot be guaranteed to provide strict upper bound solutions, our numerical results suggest that in practice the procedure will generally produce upper bounds on the exact collapse load multipliers.

Table 2
Prandtl problem: computed collapse multipliers using regular nodal layouts

Models	N: number of divisions under the indentor (total number of EFG nodes)							
	2	4	6	8	10	12	14	16
	(55)	(189)	(403)	(697)	(1071)	(1525)	(2059)	(2673)
EFG	5.2877	5.1776	5.1595	5.1528	5.1502	5.1486	5.1478	5.1473
Error (%)	2.84	0.70	0.35	0.22	0.17	0.14	0.12	0.11
CPU (s)*	0.48	0.52	0.56	0.75	1.01	1.40	2.29	5.72

*Solution time taken by MOSEK solver on a 2.8GHz Pentium 4 PC

In Table 3 the solutions obtained using the present method are compared with previously reported literature solutions. Considering previously obtained upper bound solutions, the present method provides lower (i.e. more accurate) upper bound solutions than those presented in [9,36,37]. The solution obtained using the finest nodal discretization presented used here is also lower than the best upper bound presented in [37] using a mesh of up to 18719 six-node triangle elements, and generated using a mesh with reduced element size near the indentor. In comparison with the smoothed finite element method (SFEM) solution presented in [12], the best solution presented here is higher (i.e. less accurate), although a far smaller number of nodes are employed here (2673 EFG nodes compared with 10465 SFEM nodes).

The pattern of plastic energy dissipation and collapse mechanism corresponding to the present EFG solution are shown in Figure 4(a) and 4(b) respectively.

Table 3
Prandtl problem: comparison with literature solutions

Approach	Authors	Collapse multiplier	Error (%)
Kinematic	Vicente da Silva and Antao [36]	5.264	+2.38
	Sloan & Kleeman [9]	5.210	+1.33
	Makrodimopoulos & Martin [37]	5.148	+0.12
	Le et al. [12]	5.143	+0.03
	Present method	5.147	+0.11
Analytical solution	Prandtl [35]	$2 + \pi$	–
Mixed formulation	Capsoni & Corradi [5]	5.240	+1.91
Static	Makrodimopoulos & Martin [38]	5.141	-0.01

5.2 Notched tensile specimen

The double notched tensile specimen problem was originally considered by Nagtegaal et al. [1] in order to illustrate the locking phenomena, and has since become a popular benchmark, particularly in the field of rigid-plastic limit analysis [39–41]. The problem consists of a rectangular specimen with two external thin symmetric cuts under in-plane tensile stresses τ_0, as shown in Figure 5. Taking advantage of symmetry, only the upper-right quarter of the specimen needs to be modelled (Figure 5).

The problem was solved using both regular and irregular nodal distributions, as shown on Figure 6. The degree of irregularity of interior node placement is controlled by

$$\begin{aligned} x' &= x + r \cdot \alpha_{ir} \cdot \Delta x \\ y' &= y + r \cdot \alpha_{ir} \cdot \Delta y \end{aligned} \tag{32}$$

where $r \in [-1,\ 1]$ is a computer-generated random number, the α_{ir} parameter is used to adjust the degree of nodal irregularity and Δx, Δy are initial regular nodal spacing in x and y directions respectively.

Collapse multipliers obtained using the present procedure with different nodal distributions are reported in Table 4. It can be seen that the computed collapse multiplier obtained when using a regular nodal distribution is lower than when using irregular nodal distributions. This can be explained by the fact that a

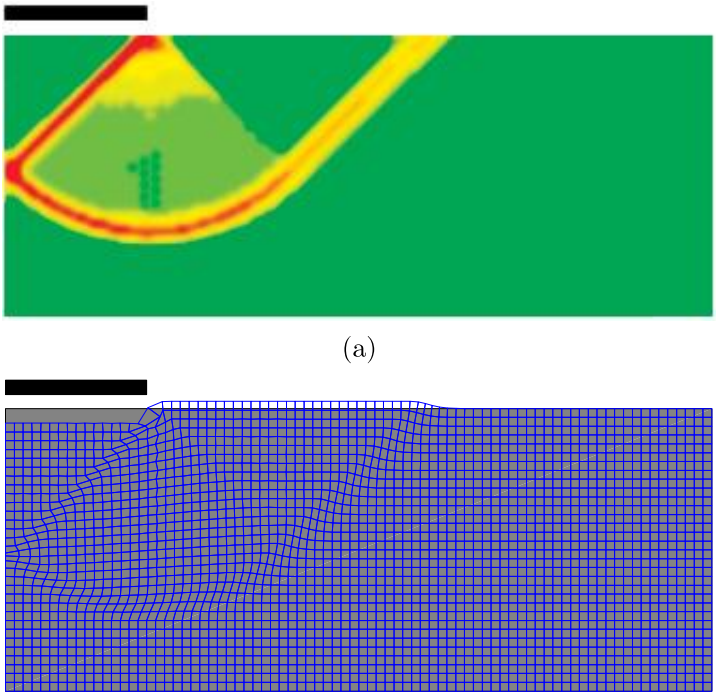

(a)

(b)

Fig. 4. Prandtl problem: (a) plastic dissipation and (b) collapse mechanism

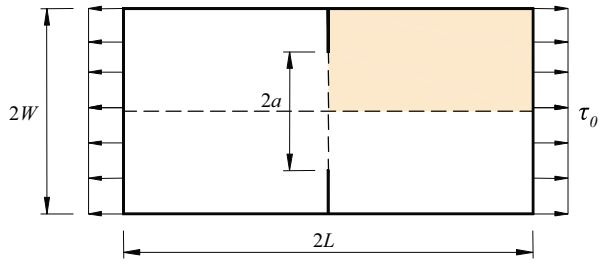

Fig. 5. Notched tensile specimen: geometry ($W = L = 1$) and loading

better (lower) collapse load multiplier is obtained if the majority of nodes are concentrated in zones where slip-lines form in the real mechanism [26], and simply distributing the nodes randomly is unlikely to achieve this.

In order to demonstrate the efficacy of the proposed method the solutions obtained using regular nodal distributions will be compared with those obtained previously. A convergence analysis is presented in Table 5, and in Table 6 the best solution obtained using the present method is compared with literature solutions. It can be observed from Table 6 that the present solutions are generally in reasonably good agreement with those obtained previously.

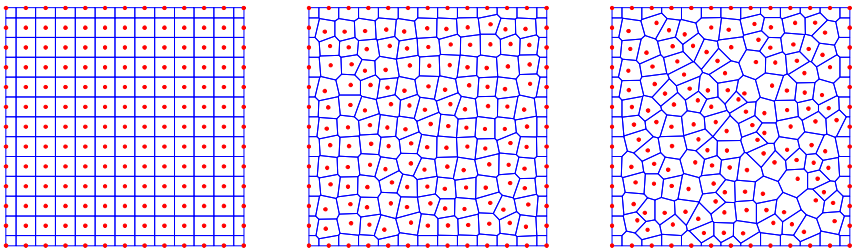

(a) (b) (c)

Fig. 6. Notched tensile specimen: nodal distribution and associated Voronoi diagrams, (a) regular, $\alpha_{ir} = 0$; (b) $\alpha_{ir} = 0.2$ and (c) $\alpha_{ir} = 0.4$

Table 4
Notched tensile specimen: influence of nodal irregularity on collapse multiplier (24×24 nodes, $a = 1/2$)

α_{ir}	0	0.1	0.2	0.3	0.4	0.5
λ^+	1.1801	1.1838	1.1850	1.1874	1.1820	1.1820
Diff. (%)*	-	+0.31	+0.42	+0.62	+0.16	+0.16

*compared with $\alpha_{ir} = 0$ case

Although the approximate upper bound solutions obtained here are slightly higher, though all within 2 percent, of those e.g. in [2,6,12], the number of primal variables (degrees of freedom) in the underlying optimisation problem is much smaller than in [2,6,12] (i.e. $2 \times 60 \times 60$ variables compared with $4 \times 240 \times 240$, $4 \times 120 \times 120$ and $2 \times 160 \times 160$ variables in [2,6,12], respectively). The solutions obtained by Christiansen and Andersen [2] and Andersen et al. [6] are widely considered as reference values, so convergence rates towards these for different values of a are illustrated in Figure 7. It is evident that the numerical solutions appear to broadly converge towards the reference values as the mesh size h tends towards zero.

The pattern of plastic energy dissipation and the collapse mechanism corresponding to the present EFG solution for the case when $a = 1/3$ are shown in Figures 8(a) and 8(b) respectively, giving a clear indication as to the form of the real slip line failure mechanism.

Table 5
Notched tensile specimen: influence of nodal density on collapse multiplier ($\alpha_{ir} = 0$)

	$a = 1/3$		$a = 1/2$		$a = 2/3$	
N	λ^+	Diff. (%)*	λ^+	Diff. (%)*	λ^+	Diff. (%)*
6	1.0662	15.4	1.3081	15.6	1.5907	15.0
12	0.9980	8.0	1.2223	8.0	1.4927	7.9
24	0.9627	4.2	1.1801	4.3	1.4411	4.2
48	0.9447	2.2	1.1581	2.3	1.4150	2.3
60	0.9412	1.9	1.1535	1.9	1.4097	1.9

*cf. results obtained by Richardson extrapolation in [2]

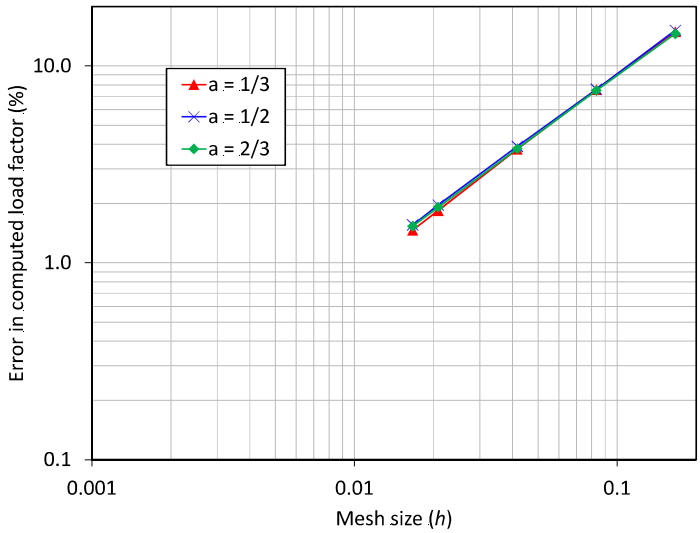

Fig. 7. Notched tensile specimen: convergence behaviour, showing approximate slope values ($\alpha_{ir} = 0$ case)

5.3 Thick clamped beam problem

The last example involves a thick clamped beam tested under plane strain conditions, of the same geometry as examined previously [5]; see Figure 9. Upper and lower bound solutions have been identified analytically by Capsoni

Table 6
Notched tensile specimen: comparison with literature solutions ($N = 60$)

Approach	Authors	$a = 1/3$	$a = 1/2$	$a = 2/3$
Kinematic	Ciria et al. [41]		1.1390	
	Le et al. [12]	0.9259	1.1374	1.3837
	Present method	0.9412	1.1535	1.4097
Mixed formulation	Christiansen and Andersen [2]	0.9276	1.1358	1.3884
	Andersen et al. [6]	0.9271	1.1366	1.3894
	Pastor et al. [7]	–	$1.1315^{low} - 1.1338^{up}$	–
Static	Ciria et al. [41]		1.1315	
	Krabbenhoft and Damkilde [42]	–	1.1315	–

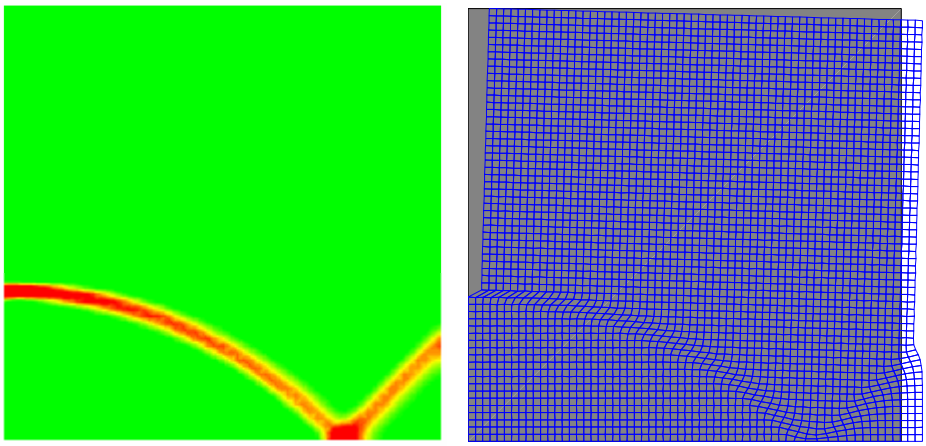

(a) (b)

Fig. 8. Notched tensile specimen: (a) plastic dissipation and (b) collapse mechanism ($a = 1/3$)

& Corradi [5] as

$$\lambda^+ = 2.0,\ \lambda^- = \begin{cases} \dfrac{4}{B+1} & \text{if } B \leq 3.828 \\ \dfrac{16}{(B-1)(B+3)} & \text{if } B \geq 3.828 \end{cases} \tag{33}$$

Symmetry means that only half the beam needs to be modelled and a discretization involving 9 nodes through the thickness of the beam was employed, comparable to the finest finite element resolution used in [5].

Collapse multipliers obtained for different values of B are shown in Figure 10. In all cases the solutions obtained using the present method were very slightly lower (better) than those obtained previously using finite elements [5]. This appears to indicate that the EFG method can provide higher accuracy for the same number of nodes used.

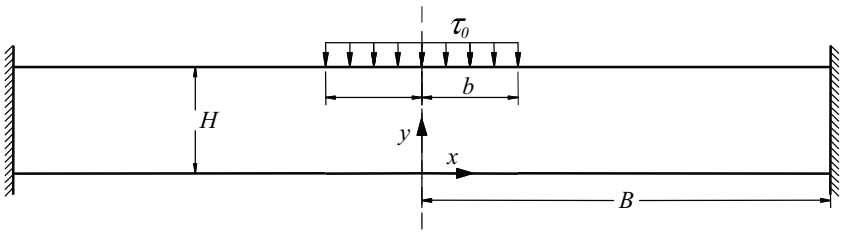

Fig. 9. Thick clamped beam: geometry and loading

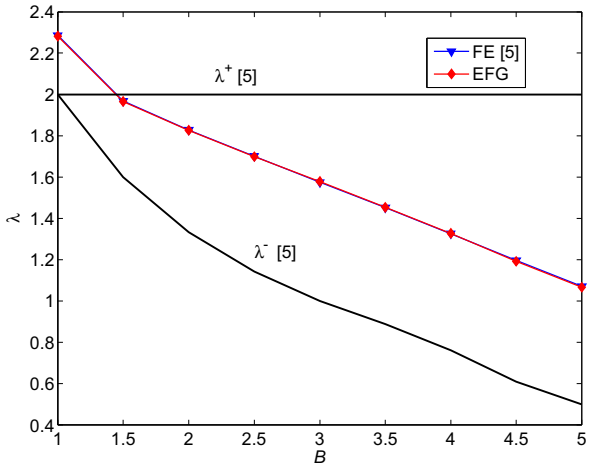

Fig. 10. Thick clamped beam: comparison of collapse multipliers

6 Conclusions

An EFG-based formulation for plane strain limit analysis problems has been described. The EFG method is used in combination with the stabilized conforming nodal integration (SCNI) scheme to ensure that volumetric locking is avoided, and that stable and accurate solutions are obtained with minimal computational effort. The discrete kinematic formulation is cast in a form

which involves second-order constraints so that the underlying optimization problem can be solved using highly efficient second-order cone programming algorithms. Although the procedure cannot be guaranteed to produce strict upper bound solutions (due to the use of somewhat relaxed compatibility conditions employed), for all the plane strain problems investigated solutions were in practice always higher than known exact solutions. To improve the accuracy of solutions and to speed-up the computational process, *a posteriori* error estimation and development of a h-adaptive EFG scheme will be the subject of future research.

Acknowledgement This research has been supported by the Vietnam National Foundation for Science and Technology Development (NAFOSTED) under grant number 107.02-2011.01.

References

1. J. C. Nagtegaal, D. M. Parks, and J. C. Rice. On numerically accurate finite element solutions in the fully plastic range. *Computer Methods in Applied Mechanics and Engineering*, 4:153–177, 1974.

2. E. Christiansen and K. D. Andersen. Computation of collapse states with von Mises type yield condition. *International Journal for Numerical Methods in Engineering*, 46:1185–1202, 1999.

3. F. Tin-Loi and N. S. Ngo. Performance of the p-version finite element method for limit analysis. *International Journal of Mechanical Sciences*, 45:1149–1166, 2003.

4. S. W. Sloan and M. F. Randolph. Numerical prediction of collapse loads using finite element methods. *International Journal for Numerical and Analytical Methods in Geomechanics*, 6:47–76, 1982.

5. A. Capsoni and L. Corradi. A finite element formulation of the rigid-plastic limit analysis problem. *International Journal for Numerical Methods in Engineering*, 40:2063–2086, 1997.

6. K. D. Andersen, E. Christiansen, and M. L. Overton. Computing limit loads by minimizing a sum of norms. *SIAM Journal on Scientific Computing*, 19:1046–1062, 1998.

7. F. Pastor, E. Loute, J. Pastor, and M. Trillat. Mixed method and convex optimization for limit analysis of homogeneous gurson materials: a kinematical approach. *European Journal of Mechanics-A/Solids*, 28:25–35, 2009.

8. A. Bottero, R. Negre, J. Pastor, and S. Turgeman. Finite element method and limit analysis theory for soil mechanics problems. *Computer Methods in Applied Mechanics and Engineering*, 22:131–149, 1980.

9. S. W. Sloan and P. W. Kleeman. Upper bound limit analysis using discontinuous velocity fields. *Computer Methods in Applied Mechanics and Engineering*, 127:293–314, 1995.

10. A. V. Lyamin and S. W. Sloan. Upper bound limit analysis using linear finite elements and nonlinear programming. *International Journal for Numerical and Analytical Methods in Geomechanics*, 26:181–216, 2002.

11. C. C. Smith and M. Gilbert. Application of Discontinuity Layout Optimization to Plane Plasticity Problems. *Proc. R. Soc. A.*, 463:2461–2484, 2007.

12. C.V. Le, H. Nguyen-Xuan, H. Askes, S. Bordas, T. Rabczuk, and H. Nguyen-Vinh. A cell-based smoothed finite element method for kinematic limit analysis. *International Journal for Numerical Methods in Engineering*, 83:1651–1674, 2010.

13. T. Belytschko, Y. Y Lu, and L. Gu. Element-Free Galerkin methods. *International Journal for Numerical Methods in Engineering*, 37:229–256, 1994.

14. S. Chen, Y. Liu, and Z. Cen. Lower-bound limit analysis by using the EFG method and non-linear programming. *International Journal for Numerical Methods in Engineering*, 74:391–415, 2008.

15. C. V. Le, M. Gilbert, and H. Askes. Limit analysis of plates using the EFG method and second-order cone programming. *International Journal for Numerical Methods in Engineering*, 78:1532–1552, 2009.

16. C. V. Le, M. Gilbert, and H. Askes. Limit analysis of plates and slabs using a meshless equilibrium formulation. *International Journal for Numerical Methods in Engineering*, 83:1739–1758, 2010.

17. H. Askes, R. de Borst, and O. Heeres. Condition for locking-free elasto-plastic analyses in the Element-Free Galerkin method. *Computer Methods in Applied Mechanics and Engineering*, 173:99–109, 1999.

18. W.K. Liu, S. Jun, and Y.F. Zhang. Reproducing kernel particle methods. *International Journal for Numerical Methods in Fluids*, 20:1081–1106, 1995.

19. J. Dolbow and T. Belytschko. Volumetric locking in the Element-Free Galerkin method. *International Journal for Numerical Methods in Engineering*, 46:925–942, 1999.

20. J.S. Chen, S. Yoon, H.P. Wang, and W.K. Liu. An improved reproducing kernel particle method for nearly incompressible finite elasticity. *Computer Methods in Applied Mechanics and Engineering*, 181:117–145, 2000.

21. A. Huerta and S. Fernandez-Mendez. Locking in the incompressible limit for the Element Free Galerkin method. *International Journal for Numerical Methods in Engineering*, 51:1361–1383, 2001.

22. S. Beissel and T. Belytschko. Nodal integration of the element-free Galerkin method. *Computer Methods in Applied Mechanics and Engineering*, 139:49–74, 1996.

23. D. Wang and J. S. Chen. Locking-free stabilized conforming nodal integration for meshfree Mindlin-Reissner plate formulation. *Computer Methods in Applied Mechanics and Engineering*, 193:1065–1083, 2004.

24. J. S. Chen, C. T. Wux, S. Yoon, and Y. You. A stabilized conforming nodal integration for Galerkin mesh-free methods. *International Journal for Numerical Methods in Engineering*, 50:435–466, 2001.

25. K. Y. Sze, J. S. Chen, N. Sheng, and X. H. Liu. Stabilized conforming nodal integration: exactness and variational justification. *Finite Elements in Analysis and Design*, 41:147–171, 2004.

26. C. V. Le, H. Askes, and M. Gilbert. Adaptive Element-Free Galerkin method applied to the limit analysis of plates. *Computer Methods in Applied Mechanics and Engineering*, 199:2487–2496, 2010.

27. C.V. Le, M. Gilbert, and Askes H. Meshless methods for upper bound and lower bound limit analysis of thin plates. In *B.H.V. Topping, J.M. Adam, F.J. Pallarés, R. Bru and M.L. Romero, (Editors), 'Developments and Applications in Computational Structures Technology'*, pages 145–168. Saxe-Coburg Publications, Stirlingshire, UK, 2010.

28. E. Christiansen. *Limit analysis of collapse states.* Handbook of Numerical Analysis, Elsevier Science B.V., 1996.

29. L.A. Mihai and M. Ainsworth. A finite element procedure for rigorous numerical enclosures on the limit load in the analysis of multibody structures. *Computer Methods in Applied Mechanics and Engineering*, 199:48–60, 2009.

30. P. V. Nguyen, T. Rabczuk, S. Bordas, and M. Duflot. Meshless methods: A review and computer implementation aspects. *Mathematics and Computers in Simulation*, 79:763–813, 2008.

31. J. S. Chen, C. T Wu, and T. Belytschko. Regularization of material instabilities by meshfree approximations with intrinsic length scales. *International Journal for Numerical Methods in Engineering*, 47:1303–1322, 2000.

32. J. W. Yoo, B. Moran, and J. S Chen. Stabilized conforming nodal integration in the natural-element method. *International Journal for Numerical Methods in Engineering*, 60:861–890, 2004.

33. C.V. Le. *Novel numerical procedures for limit analysis of structures – meshfree methods and mathematical programming.* PhD thesis, University of Sheffield, 2010.

34. T. Zhu and S. N. Atluri. A modified collocation method and a penalty formulation for enforcing the essential boundary conditions in the element free Galerkin method. *Computational Mechanics*, 21:211–222, 1998.

35. L. Prandtl. Ueber die Haerte plastischer Koerper. *Nachrichtex der Akademie der Wissenschaften in Gottingen. II. Mathematisch-Physikalische Klasse II*, 12:74–85, 1920.

36. M. Vicente da Silva and A. N. Antao. A non-linear programming method approach for upper bound limit analysis. *International Journal for Numerical Methods in Engineering*, 72:1192–1218, 2007.

37. A. Makrodimopoulos and C. M. Martin. Upper bound limit analysis using simplex strain elements and second-order cone programming. *International Journal for Numerical and Analytical Methods in Geomechanics*, 31:835–865, 2006.

38. A. Makrodimopoulos and C. M. Martin. Lower bound limit analysis of cohesive-frictional materials using second-order cone programming. *International Journal for Numerical Methods in Engineering*, 66:604–634, 2006.

39. E. Christiansen and O. S. Pedersen. Automatic mesh refinement in limit analysis. *International Journal for Numerical Methods in Engineering.*, 50:1331–1346, 2001.

40. K. Krabbenhoft and L. Damkilde. A general nonlinear optimization algorithm for lower bound limit analysis. *International Journal for Numerical Methods in Engineering*, 56:165–184, 2003.

41. H. Ciria, J. Peraire, and J. Bonet. Mesh adaptive computation of upper and lower bounds in limit analysis. *International Journal for Numerical Methods in Engineering.*, 75:899–944, 2008.

42. K. Krabbenhoft and L. Damkilde. A general nonlinear optimization algorithm for lower bound limit analysis. *International Journal for Numerical Methods in Engineering*, 56:165–184, 2003.